New Experimental Single-Axis Excitation Set-Up for Multi-Axial Random Fatigue Assessments

machines

MDPI

Article

New Experimental Single-Axis Excitation Set-Up for Multi-Axial Random Fatigue Assessments

Luca Campello [1,2], Vivien Denis [2], Raffaella Sesana [1,*], Cristiana Delprete [1] and Roger Serra [2]

[1] Department of Mechanical and Aerospace Engineering (DIMEAS), Politecnico di Torino, Corso Duca Degli Abruzzi 24, 10129 Turin, Italy; luca.campello@polito.it (L.C.); cristiana.delprete@polito.it (C.D.)
[2] Mechanics Laboratory G. Lamé (LaMé), INSA Centre Val de Loire, 3 rue de la Chocolaterie, 41000 Blois, France; vivien.denis@insa-cvl.fr (V.D.); roger.serra@insa-cvl.fr (R.S.)
* Correspondence: raffaella.sesana@polito.it

Abstract

Fatigue failure, generated by local multi-axial random state stress, frequently occurs in many engineering fields. Therefore, it is customary to perform experimental vibration tests for a structural durability assessment. Over the years, a number of testing methodologies, which differ in terms of the testing machines, specimen geometry, and type of excitation, have been proposed. The aim of this paper is to describe a new testing procedure for random multi-axial fatigue testing. In particular, the paper presents the experimental set-up, the testing procedure, and the data analysis procedure to obtain the multi-axial random fatigue life estimation. The originality of the proposed methodology consists in the experimental set-up, which allows performing multi-axial fatigue tests with different normal-to-shear stress ratios, by choosing the proper frequency range, using a single-axis exciter. The system is composed of a special designed specimen, clamped on a uni-axial shaker. On the specimen tip, a T-shaped mass is placed, which generates a tunable multi-axial stress state. Furthermore, by means of a finite element model, the system dynamic response and the stress on the notched specimen section are estimated. The model is validated through a harmonic acceleration base test. The experimental tests validate the numerical simulations and confirm the presence of bending–torsion coupled loading.

Keywords: dynamical response; spectral fatigue analysis; damage analysis; finite element analysis

Academic Editor: Candida Petrogalli

Received: 8 May 2025
Revised: 7 June 2025
Accepted: 17 June 2025
Published: 20 June 2025

Citation: Campello, L.; Denis, V.; Sesana, R.; Delprete, C.; Serra, R. New Experimental Single-Axis Excitation Set-Up for Multi-Axial Random Fatigue Assessments. *Machines* **2025**, *13*, 539. https://doi.org/10.3390/machines13070539

1. Introduction

Mechanical components may be subjected to a wide spectrum of time-varying fatigue loading such as non-proportional cyclic loading, asynchronous cyclic loading, complex loading paths, mean stresses, varying stress amplitudes, and random loading [1]. Often randomly, situations where the stress value varies can frequently occur, under the action of wind or sea or because of vibrations. These kinds of conditions can be found in many engineering fields like the automotive, aerospace, railway, naval, etc.

To estimate the component life, structural durability assessment in the pre-design phase is a common approach, often with the aid of finite element analysis (FEA). The features of fatigue failure are based on the material parameters, as reported by Sonsino [2], which are extracted from simplified experimental laboratory tests. Such tests are executed applying uni-axial or multi-axial constant amplitude loadings (e.g., axial, bending, or torsion) on standard or notched specimens, characterizing the fatigue strength material

behavior in terms of the stress S versus the number of cycles to failure N (Schijve [1]). The characterization of uniform and multiaxial constant amplitude fatigue of materials rely on a large number of standards and specifications (ASTM [3], ISO [4], DIN [5]), indicating the testing procedures. Cumulative fatigue damage analysis plays a key role in the life evaluation of structural components exposed to load histories. According to Fatemi and Young [6], for a fatigue damage assessment in the situation of constant amplitude vibration, a large number of fatigue damage accumulation models are available.

The crucial point is that real in-service time-varying loadings are often random and associated with a multi-axial stress state (Liu et al. [7], Shen et al. [8]). Therefore, to evaluate the fatigue strength of a component, multi-axial life and damage estimation criteria are required. In the literature, several models are presented to estimate the damage and the fatigue life for multiaxial random loads, based on different approaches, such as the critical plane, stress invariant (Mrnik et al. [9], Carpinteri et al. [10]), or energy-based (Braccesi et al. [11], Pitoiset and Preumont [12]). Despite the improvement in the theoretical and numerical analyses, the life cycle prediction under multi-axial dynamic loading requires experimental validation and the design of appropriate test specifications. Creating a test specification to evaluate the fatigue damage produced by vibration in the real environment remains a challenging goal. The current ability to perform multi-axial fatigue tests is adversely affected by the complexity of the testing equipment and procedures, as reported by Habtour et al. [13].

In the light of the aforementioned considerations, the life of metallic structures is commonly evaluated by employing a uni-axial fatigue test with a simple cantilever beam, producing a uni-axial bending stress state (Appert et al. [14], Ghielmetti et al. [15], Paulus et al. [16], de M. Teixeira [17]). However, as a compromise, military and commercial standards propose conducting vibration tests by applying uni-axial excitation to test articles along three orthogonal axes sequentially. Whiteman and Berman [18], Whiteman and Berman [19], French et al. [20] have shown that these procedures do not provide vibration profiles for simultaneous multi-axial vibration. In fact, uni-axial input does not excite a stress state that is likely to exist in a true operational environment with multi-axis input, which excites all modes simultaneously and induces a more realistic vibration stress loading condition (Nath and Aglietti [21], Zheng et al. [22]). Due to this, uni-axial test procedures lead to an overestimation of the component's fatigue life.

The stress state in fatigue testing may vary according the shape of the geometry and the layout of the testing system (Marques et al. [23]). In the case of plate specimens, some particular geometries have been proposed (Morettini et al. [24], Morettini et al. [25], Claudio et al. [26], George et al. [27]), where a bi-axial stress state is produced. The best way to reach a multi-axial stress state with both normal and shear stresses is the use of cylindrical specimens.

A significant improvement to testing equipment could be made by exciting the structure at multiple locations with different electrodynamic shakers and controlling the vibration test at multiple response locations using a Multi-Input–Multi-Output (MIMO) vibration control technology (Daborn et al. [28]). By adopting this solution, fatigue tests can be performed achieving bending–torsion loadings using two independent uni-axial shakers, one mounted to an arm parallel to the specimen and the second mounted to an arm perpendicular to the specimen (Lagoda et al. [29]). This layout could be a good reproduction of multi-axial excitation environments. In addition, the system yields a pure bending loading when only the arm parallel to the specimen axis is excited by a uni-axial shaker. Imposing the loading with the other shaker, the specimen is subjected to a torsion loading condition.

By adding two tipped masses to a cylindrical specimen mounted over a uni-axial shaker, it is possible to obtain a bending-torsion loading in the specimen. In this case, the load components are always coupled (Nguyen et al. [30]). Zanellati et al. [31] propose another layout, a special holder structure designed to independently control bending and torsion loadings. It was designed to decouple the bending and torsion, but it needs a three-axis shaker.

In some other cases, more elaborated specimens have been developed with the aim of performing accelerated fatigue tests using shaker tables and simulating an actual operating scenario of complex structures like a Y-shaped specimen with two tipped masses, which develop a multi-axial stress when subjected to a uni-axial base excitation (Cesnik et al. [32]).

Thus, to overcome these limitations, in the present paper, a new testing set-up is presented, inspired by Rognon [33]. It enables the application of a coupled torsional and bending deformation by means of a uni-axial excitation shaker; depending on the mode that is excited, the ratio torsion/bending deformation can change. The experimental system comprises a dedicated designed specimen, clamped on a uni-directional shaker and a T-shaped mass (T-mass) tied to the free end of the specimen. The purpose of this study is to describe the proposed set-up, the experimental testing procedure, and the validation of the system and the procedure when evaluating the fatigue life over random vibrations of a metallic material, comparing the obtained results with well-known numerical models.

2. Theoretical Background

In this section, the theoretical background is presented to deal with random stress tensor and fatigue analysis in the frequency domain. Detailed descriptions can be found in Bendat and Piersol [34], Maia et al. [35], Niesłony and Macha [36], and Socie [37].

2.1. Dynamic Analysis and the Resulting Stress State in Random Loadings

In accelerated vibration tests using an electrodynamic shaker, the motion of a given dynamic structure, excited by a base acceleration $\ddot{\mathbf{x}}_0(\omega)$, can be described as follows (Cesnik et al. [38]):

$$(\mathbf{K} - \omega^2\mathbf{M} + i\omega\mathbf{C})\mathbf{y}(\omega) = \mathbf{M}\ddot{\mathbf{x}}_0(\omega), \tag{1}$$

where $\mathbf{y}$ is the vector of the displacement response of the dynamic structure, ω is the excitation frequency, and $\mathbf{M}, \mathbf{C}, \mathbf{K}$ are, respectively, the mass matrix, the damping matrix, and the stiffness matrix of the vibrating system.

The solution of the eigenvalue problem gives the eigenfrequencies and eigenmodes, characterizing the dynamic behaviour of the structure. Thanks to the superposition approach, Equation (1) can be rearranged in Equation (2) as

$$\mathbf{y}(\omega) = \mathbf{H}(\omega)\mathbf{M}\ddot{\mathbf{x}}_0(\omega), \tag{2}$$

where $\mathbf{H}$, defined as the transfer-function matrix, relates the kinematic excitation to the displacement responses.

For the purposes of the fatigue analysis, a transfer matrix can be defined, Equation (3), as the stress frequency-response Function, relating the kinematic excitation to the stress response of the structure (Kranjc et al. [39]) and it is computed as

$$\mathbf{H_{as}}(\omega) = \sum_{r=1}^{n} \frac{\mathbf{A_r^s}}{\omega_r^2 - \omega^2 + i\eta_r\omega\omega_r}, \tag{3}$$

where ω_r is the r-th natural frequency, η_r is the modal damping loss factor for the r-th natural frequency, and $\mathbf{A_r^s}$ is a stress modal constants matrix, defined by Mršnik et al. [40].

In tests with multi-axial random loadings, the stress distribution at a given point can be characterised in the frequency domain by a stress–power spectral density (stress-PSD) matrix $\mathbf{S_s}(\omega)$ (Equation (4)), computed as

$$\mathbf{S_s}(\omega) = \mathbf{H_{as}}(\omega)^T \mathbf{S_{in}}(\omega) \mathbf{H_{as}}(\omega), \tag{4}$$

where $\mathbf{S_{in}}(\omega)$ is the input acceleration–PSD matrix.

The stress-PSD matrix $\mathbf{S_s}(\omega)$ takes the form of a 6×6 matrix (Equation (5)):

$$\mathbf{S_s}(\omega) = \begin{pmatrix} S_{xx,xx}(\omega) & \dots & S_{xx,yz}(\omega) \\ \vdots & \ddots & \vdots \\ S_{yz,xx}(\omega) & \dots & S_{yz,yz}(\omega) \end{pmatrix}. \tag{5}$$

The diagonal terms $S_{ii}(\omega)$ in the PSD matrix represent the auto-spectral density functions, whereas the off-diagonal terms $S_{ij}(\omega)$ represent the cross-spectral density functions (Jang and Park [41]).

2.2. Multi-Axial Criteria

To carry out fatigue assessment in a component under multi-axial loading, an equivalent stress component is required to reduce the stress component to a more manageable form from Equation (5) into an equivalent stress–PSD $S_{eq}(\omega)$. The criterion proposed by Preumont and Piefort [12] is one of the frequently used frequency-domain methods for the equivalent-stress calculation due to the simplicity of the approach (Mršnik et al. [9]).

Preumont and Piefort [42] reformulated a new equivalent von Mises stress (EVMS) in the frequency domain:

$$S_{eq}(\omega) = \int_0^\infty Tr\{\mathbf{Q}\mathbf{S_s}(\omega)\} d\omega, \tag{6}$$

where $Tr\{\}$ is the trace function, and $\mathbf{Q}$ is the coefficient matrix defined as

$$\mathbf{Q} = \begin{pmatrix} 1 & -1/2 & -1/2 & 0 & 0 & 0 \\ -1/2 & 1 & -1/2 & 0 & 0 & 0 \\ -1/2 & -1/2 & 1 & 0 & 0 & 0 \\ 0 & 0 & 0 & 3 & 0 & 0 \\ 0 & 0 & 0 & 0 & 3 & 0 \\ 0 & 0 & 0 & 0 & 0 & 3 \end{pmatrix}. \tag{7}$$

2.3. Fatigue Life Assessment

After determining the equivalent stress–PSD $S_{eq}(\omega)$ using the uni-axial random approach together with established spectral methods, a fatigue life evaluation can be performed. Under the hypothesis of a linear damage-accumulation law based on the Palmgreen and Miner rule [43], the expected fatigue damage per unit time $E[D]$ may be evaluated, using the so-called NarrowBand approach (Mršnik et al.) [44]:

$$E(D) = \nu_p C^{-1} \left(\sqrt{2m_0}\right)^k \Gamma\left(1 + \frac{k}{2}\right), \tag{8}$$

where $E(D)$ is the expected fatigue damage for the unit time. C and k are material parameters characterising the SN curve, which relate the stress amplitude σ_i and the number of cycles before failure N_i, according to Basquin's equation, Equation (9) (Milella [45]):

$$N\sigma_i^k = C. \tag{9}$$

m_0 is the zero spectral moment, Γ is the Euler Gamma function, and ν_p is the expected peak rate of the signal in the time domain (Equation (10)):

$$\nu_p = \sqrt{\frac{m_4}{m_2}}, \tag{10}$$

where m_2 and m_4 are, respectively, the second and fourth spectral moments.

All the spectral moments can be computed according Equation (11):

$$m_i = \int_0^{+\infty} \omega^i S_{eq}(\omega) d\omega, \tag{11}$$

and the Euler gamma function (Equation (12)) is defined as

$$\Gamma(z) = \int_0^{(\infty)} t^{z-1} e^{-t} dt. \tag{12}$$

By considering the critical damage equal to the unity, the calculated fatigue life T in seconds is

$$T = \frac{1}{E(D)}. \tag{13}$$

3. Testing Layout

The proposed testing set-up system comprises a T shaped mass clamped on the free end of a specimen, whose geometry is described and analysed in Nagulapalli et al. [46]. The specimen is clamped on an electromagnetic shaker. The T-mass is added with the aim of tuning the bending–torsion stress contribution. In addiction, two uni-axial accelerometers are used for the experimental analysis. In the present paper, specimens are made of Complex Phase 800 steel. The mechanical properties of the two components (specimen and T-mass) are summarized in Table 1.

Table 1. Mechanical properties of the testing set-up components.

Component	Material	*E* [GPa]	Density [kg/m^3]
Specimen	Steel	200	7740
T-mass	Aluminum	72	2715

Figure 1 shows the geometrical dimensions of the specimen, while the geometrical dimensions of the T-mass are presented and discussed in Section 4.1.

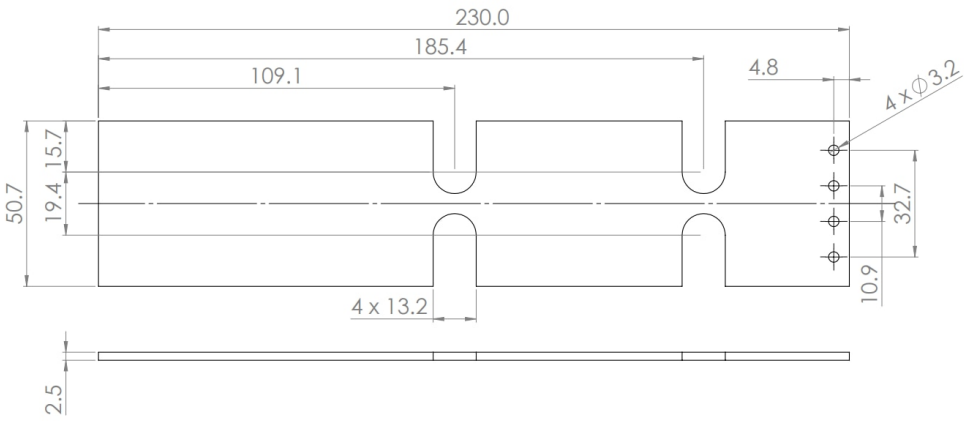

Figure 1. Geometrical dimensions of the specimen in millimeters.

4. Numerical Simulation

The aim of the numerical analysis was the evaluation of the dynamic behaviour and stress components of the specimen. The FEM model replicated the experimental configuration and specimens, and it is reported as an example of the procedure. A sensitivity analysis to investigate the influence of T-mass geometry dimensions was performed, as reported in Section 4.1, and on the basis of the results, a configuration for a fatigue life assessment was chosen.

The FE model of the set-up is presented in Figure 2. The specimen is meshed with second order hexahedron elements, while the T-mass is meshed with first order hexahedron elements. The element size varies approximately from 5×10^{-4} m on the notches to 5×10^{-3} m on the rest of the system. The external constraints are defined using SPC (single points constrained) aiming to reproduce the clamped system, used for experimental tests, with a length of 32 mm. All the components were connected, using a TIE CONTACT. The numerical calculations were run with Altair Hyperworks software 2021 and Matlab 2024b, using a Computer with Intel Core i7 and 64 GB RAM. The total duration of the calculation was approximately 30 min.

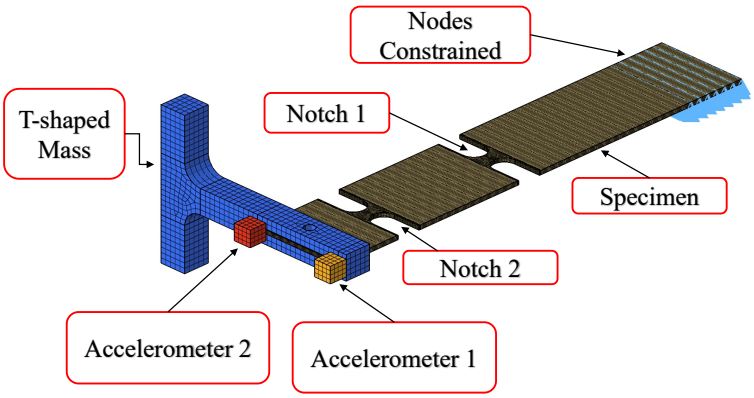

Figure 2. Numerical model of the testing set-up.

4.1. T-Mass Shaped Design Phase

Four dimensions of the T-mass were selected (*a*, *b*, *c* and *h* in Figure 3) to provide an example of a possible tool for tuning the coupling of the shear and normal stress distribution in the notched section of the specimen. The dimension *b* is the distance between the longitudinal axis of the specimen and the distal point of the T-mass, *c* is the length of the vertical part, and *a* and *h* are the width and the thickness of the horizontal part of the T-mass.

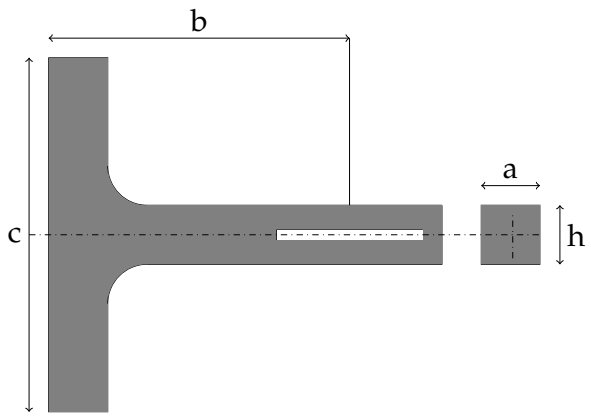

Figure 3. T-mass profile.

The analyses were conducted, increasing the dimensions b and c of about 50% and 75% in relation to the starting configuration (Table 2), as an example, to investigate how each of them contributes to the shear and normal stress distribution, to the modal shapes, and to the modal frequencies. The dimensions a and h are modified, consequently, to keep the mass of the T-mass constant at 106.9 g.

Table 2. Dimensions of the three T-mass geometrical configurations.

T-Mass Configuration	a [mm]	b [mm]	c [mm]	h [mm]	Mass [g]
1	14.9	86.7	90.0	15.0	106.9
2	11.0	130.00	135.0	12.7	106.9
3	9.5	151.73	157.5	12.0	106.9

Figure 4 shows the effects of the T-mass on the specimen dynamic behaviour, using the first testing configuration as an example. The results were obtained by running a frequency sweep with a constant acceleration of 0.1 g, where g is the gravity acceleration, from 5 Hz to 600 Hz. As depicted in the figure, without the presence of the T-mass, the bending deformation is predominant in all the resonances. On the other side, adding the T-mass, a torsional deformation appears in all the resonances, with a major contribution in the second one, where a torsional rotation emerges with the centre of rotation outside the longitudinal axis of the specimen.

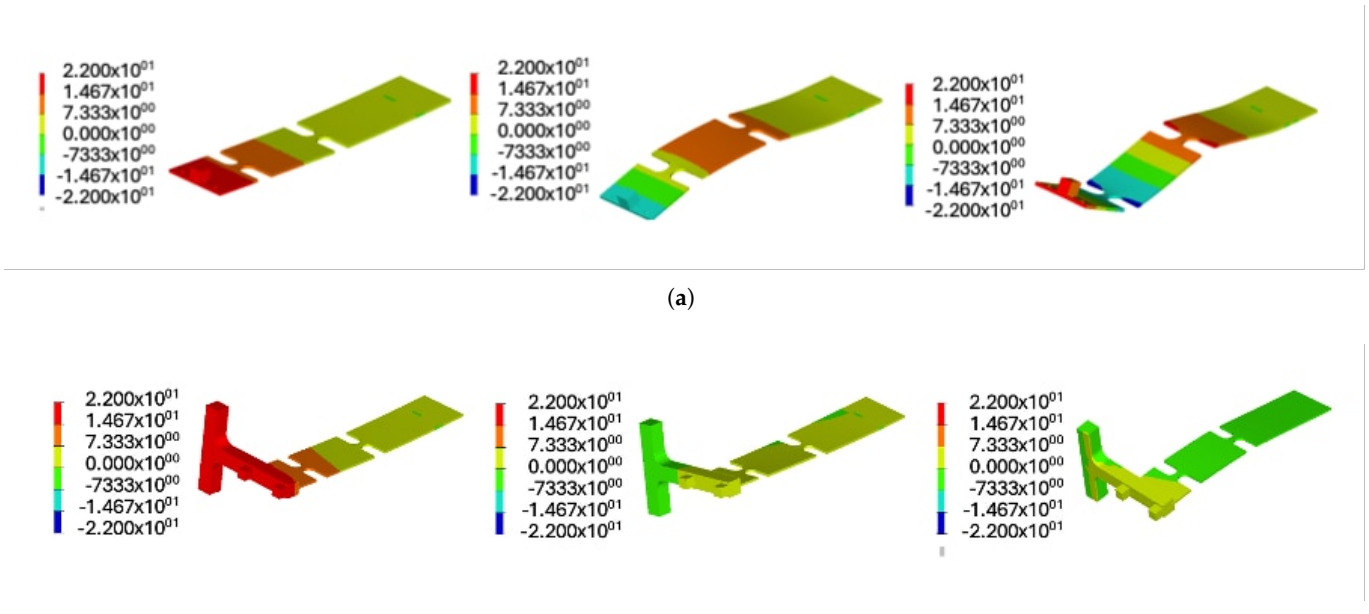

Figure 4. Acceleration results of the system in [m·s^{-2}]: (**a**) first three modes on the specimen free end, (**b**) first three modes with the T-mass.

The first step of the sensitivity analysis was the calculation and comparison of the natural frequencies and mode shapes of the system for each T-mass configuration. Figure 5 depicts the first four mode shapes obtained with the first testing configuration. As stated previously, all the four modes have a torsional deformation, but while for the first, the third, and the fourth modes a bending deformation is predominant, in the second mode, torsional deformation is more relevant. In the second mode, the asymmetry of the system leads to

a centre of rotation outside the longitudinal axis of the specimen, and as a consequence, a bending deformation is produced.

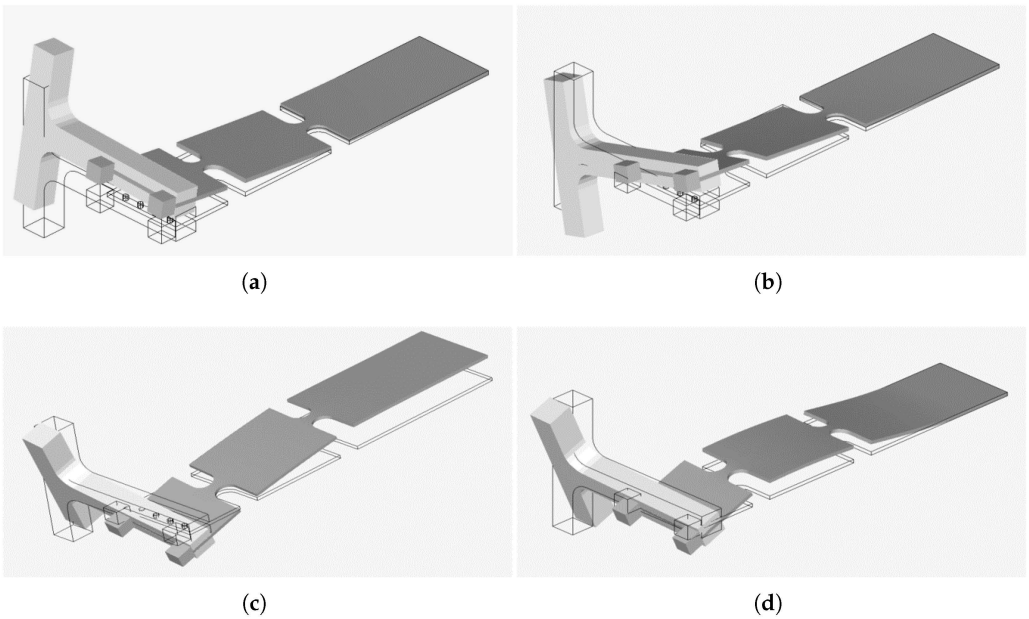

Figure 5. Mode shapes for the first system configuration: (**a**) first mode, (**b**) second mode, (**c**) third mode, (**d**) fourth mode.

As illustrated in Table 3, the term "Shift $(\pm\%)$" indicates the percent variation of frequency referred to that vibration mode. As expected, the increase in the b and c dimensions produces a decrease in frequency resonance of the first mode. The second mode is the one with a larger decrease, almost 35%, while the first mode decreases approximately 17%.

Table 3. Natural frequencies for each T-mass configuration.

	Mode 1		**Mode 2**		**Mode 3**		**Mode 4**	
	[Hz]	**Shift $(\pm\%)$**	**[Hz]**	**Shift $(\pm\%)$**	**[Hz]**	**Shift $(\pm\%)$**	**[Hz]**	**Shift $(\pm\%)$**
1	20.29		62.28		88.18		169.82	
2	17.98	−11	44.80	−28	72.59	−18	135.59	−20
3	16.82	−17	40.85	−34	63.31	−28	119.20	−30

The second step is the comparison of the modal participation factors, mathematically defined as $\mathbf{\Phi_i}^T\mathbf{M\ddot{u}}$, that quantifies the contribution of a given mode $\mathbf{\Phi_i}$ to the response of the structure when subjected to an acceleration excitation $\mathbf{\ddot{u}}$ in a given direction. In Table 4, the term "Shift $(\pm\%)$" indicates the percent variation of frequency referred to that vibration mode. The modal participation factors for each T-mass configuration are reported. The increase in the size of the T-mass leads to a reduction for the first mode and to an increase for the second mode. The fourth mode does not show any change, and it remains constant. To conclude, it is worth noting that, using the third T-mass configuration, the second and the fourth mode present values of the same order of magnitude. This means that in this T-mass configuration, the mode with coupled bending–torsion deformation has the same contribution as the mode with pure bending deformation on the response of the structure.

Table 4. Modal participation factors for each T-mass configuration.

	Mode 1	Shift (±%)	Mode 2	Shift (±%)	Mode 4	Shift (±%)
1	0.436		0.0869		0.189	
2	0.416	−4.6	0.139	60.1	0.190	0.3
3	0.340	−22.1	0.166	86.0	0.193	1.7

Considering the modal participation factors, the maximum von Mises equivalent stress for each set-up is evaluated by applying a steady acceleration of 0.981 m/s^2 across a frequency range of 30 Hz to 200 Hz, focusing solely on mode 2 and mode 4 (Table 5), as these modes represent two possible configuration of coupled normal and shear stresses and frequency ranges, which are suitable for testing activity. In the same Table 5, the term "Shift (±%)" indicates the percent variation in the von Mises stress referring to that vibration mode. The stress values are determined for the elements experiencing the highest stress. The most stressed element for mode 2 (element n. 34,625) is located in notch 1, while for mode 4, it (element n. 22,064) is located in notch 2 (Figure 6).

Table 5. Maximum von Mises stress for each T-mass configuration.

	Mode 2		Mode 4	
	[MPa]	Shift (±%)	[MPa]	Shift (±%)
1	2.98		27.35	
2	6.24	109	35	27
3	7.85	163	38.85	42

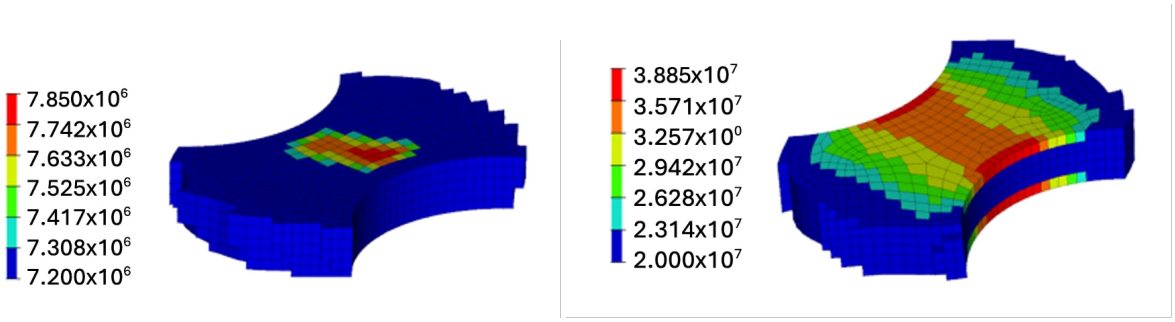

(**a**) (**b**)

Figure 6. Maximum von Mises stress distribution, in [Pa], for mode 2 in notch 1 (**a**) and for mode 4 in notch 2 (**b**).

Globally, both modes display an increase in stress levels. Mode 4 has the highest stress in every configuration. The second mode increases from 2.98 MPa to 6.24 MPa, an increase of 109% in the second T-mass configuration, and to 7.85 MPa, an increase of 163% in the third T-mass configuration. The fourth mode, compared to the second, shows a lower increase, from 34 MPa to 43.20 MPa, an increase of 27%, in the second T-mass configuration, and to 48.41 MPa.

Considering the effect on modal participation factors, the third T-mass configuration was chosen for conducting the fatigue analysis (Figure 7). It is necessary to point out that the previous analysis depends on the geometry of the specimen. Therefore, when a new geometry is used, different results and different conclusions might be achieved.

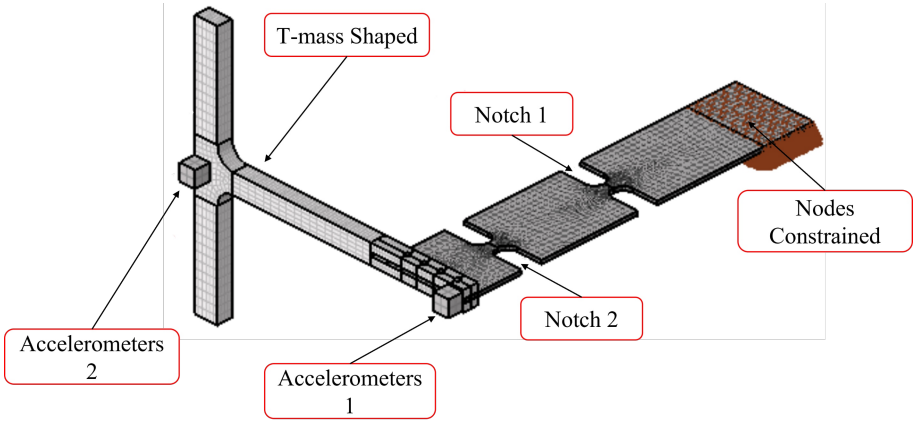

Figure 7. Third configuration for the testing set-up.

4.2. Dynamic Evaluation

Natural frequencies (Table 6), displacements mode shapes (Figure 8), and stress mode shapes (Figure 9) of the third T-mass configuration were extracted for this specific testing configuration, as an example.

Table 6. Natural frequencies for the third T-mass configuration.

Mode	Frequency [Hz]	Deformation
1	16.9	bending
2	40.85	torsional–bending
3	63.31	bending
4	119.82	bending

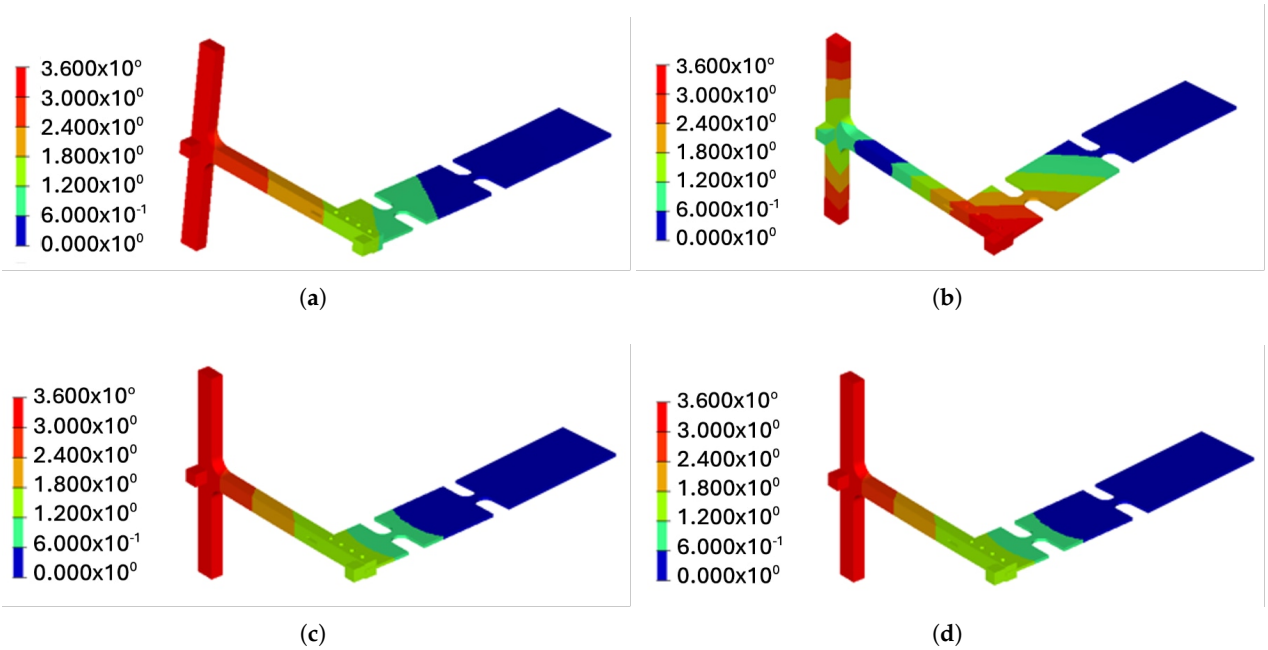

Figure 8. Displacement mode shapes for the third T-mass configuration: (**a**) mode 1, (**b**) mode 2, (**c**) mode 3, (**d**) mode 4.

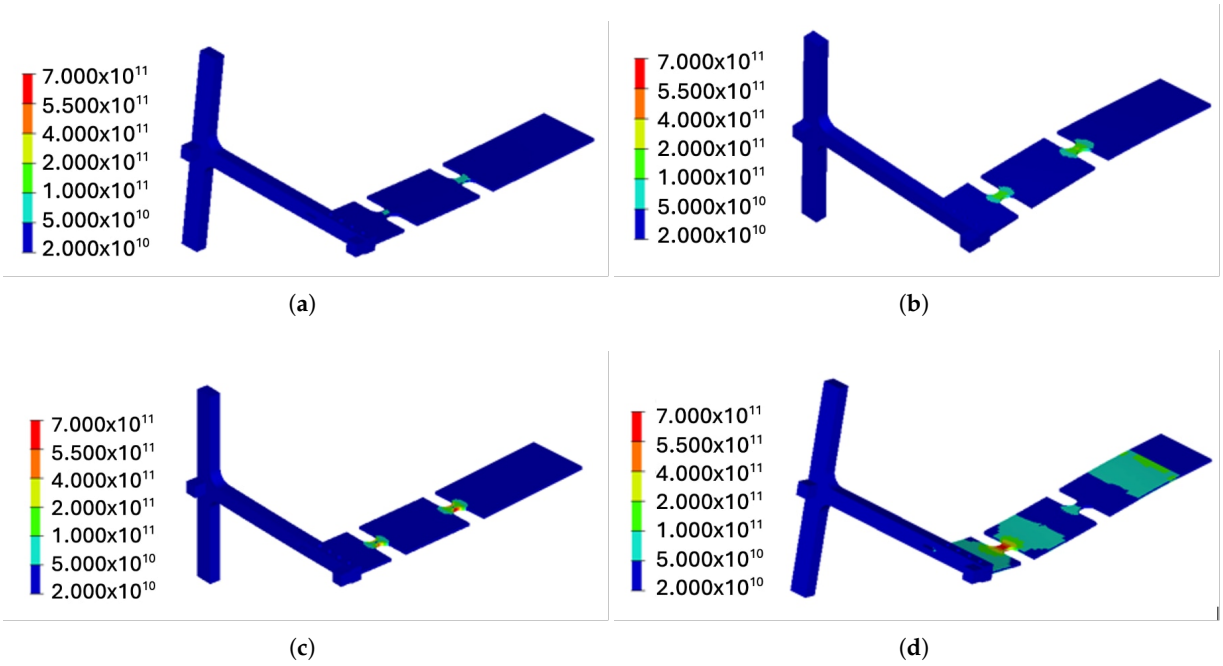

Figure 9. Stress mode shapes for the third T-mass configuration: (**a**) mode 1, (**b**) mode 2, (**c**) mode 3, (**d**) mode 4.

A numerical frequency response function is obtained in a frequency range from 20 Hz to 150 Hz with an acceleration level of 0.1 g. The calculated modal damping values for mode 2 and mode 4 are summarized in Table 7. It was calibrated after the experimental part, illustrated in Section 5.

Table 7. Calculated modal damping.

Mode	ζ [%]
2	3
4	1.5

Figure 10a depicts the numerical acceleration response of the two accelerometer components. A torsional contribution is present in both modes, given that, in the case of pure bending deformation, the two accelerometers would have shown the same acceleration at the resonance peaks. Table 8 illustrates the maximum acceleration of the accelerometers for each mode.

Figure 10b shows the stress components for mode 2 and mode 4, computed on their own most stressed elements. From what is depicted, σ_{xx} and τ_{xy} are the only only remarkable stress components in mode 2, which proves the specimen is under torsional–bending deformation. However, in mode 4, σ_{xx} is the only worthwhile stress component, confirming the specimen is subjected to pure bending deformation.

Table 8. Numerical acceleration peaks for the second and fourth mode.

	Mode 2	Mode 4
Accelerometer 1 [g]	1	1.3
Accelerometer 2 [g]	0.34	2.2

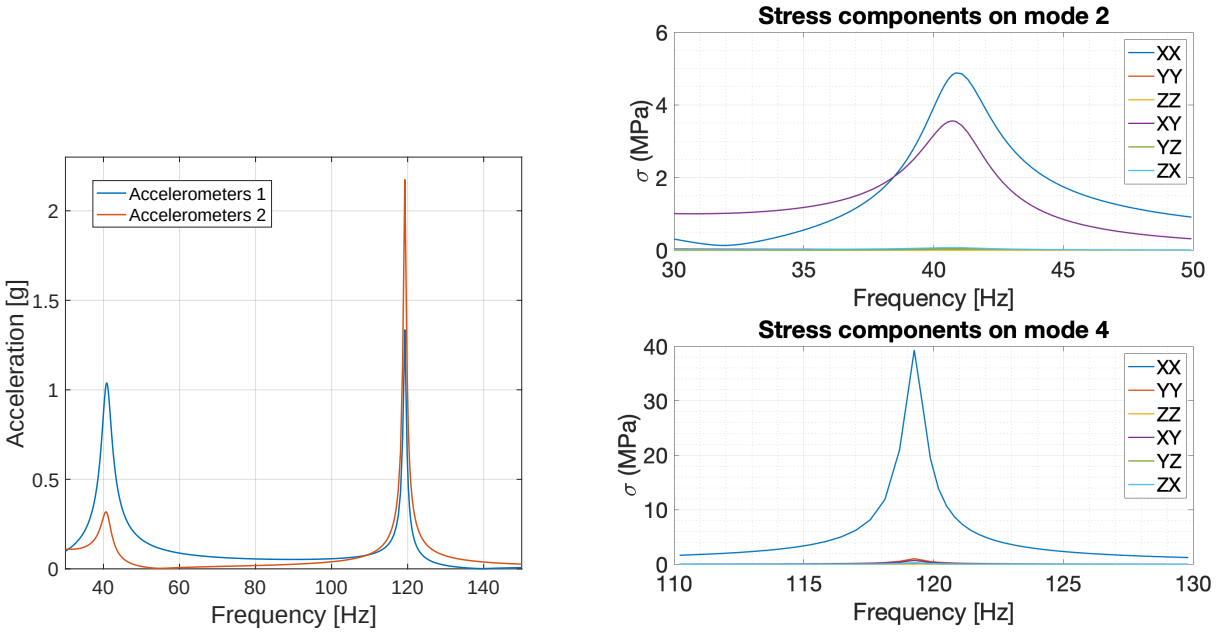

(**a**) (**b**)

Figure 10. Results of the numerical dynamic analysis: (**a**) numerical acceleration response from the two accelerometers' numerical components, (**b**) numerical stress components for mode 2 (**upper**) and mode 4 (**lower**) on their most stressed elements.

4.3. Fatigue Analysis

Six different bandwidth-limited white noise PSDs were used as load input, three for each of the two resonant modes, centered around the frequency resonance, with a range width of 20 Hz, as illustrated in Table 9 and Figure 11. In Figure 12 the equivalent power spectral density for second mode and fourth mode is plotted for the corresponding most stressed elements.

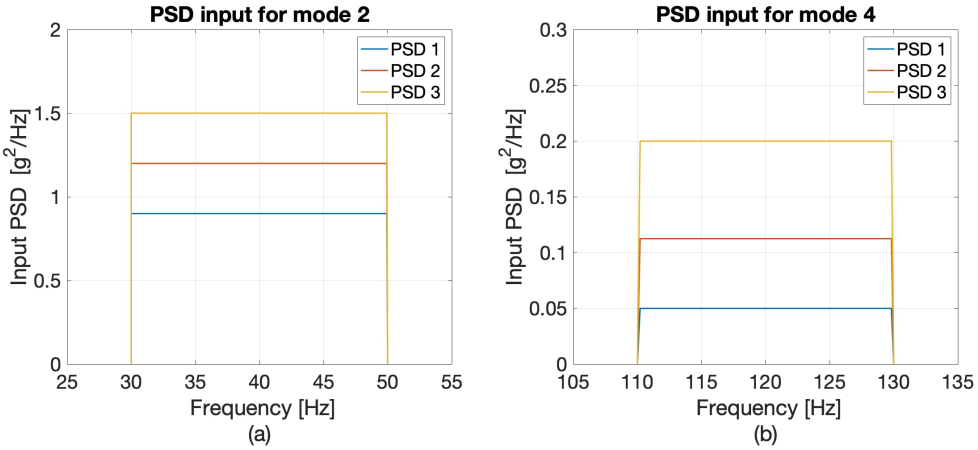

Figure 11. PSD input for second (**a**) and fourth modes (**b**).

Table 9. PSD load level according the mode shapes.

	Mode 2			**Mode 4**		
PSD [$g^2 \cdot Hz^{-1}$]	0.9	1.2	1.5	0.05	0.112	0.2
RMS [g]	4.2	4.9	5.5	1	1.5	2

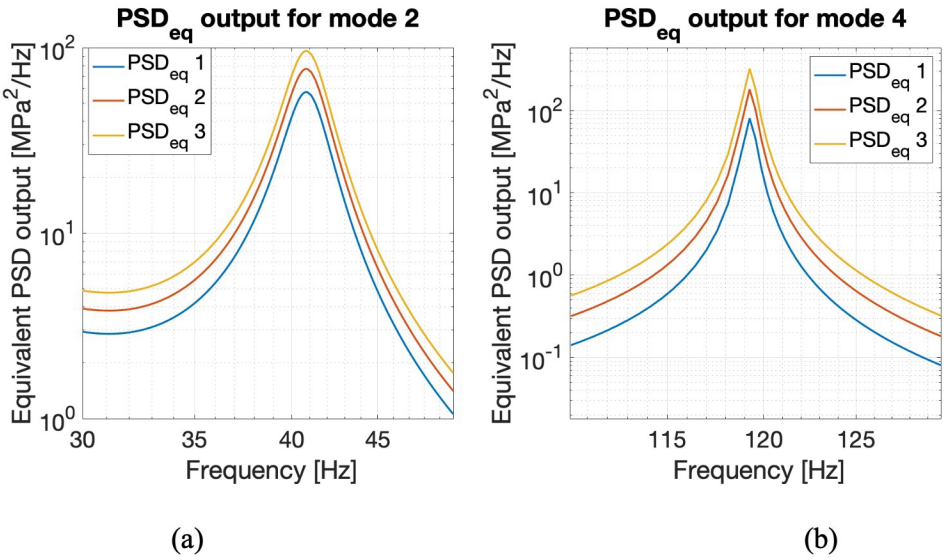

Figure 12. Equivalent power spectral density for second mode (**a**) and fourth mode (**b**) for their own most stressed elements.

By means of Equation (4) and the stress frequency response function, the stress–PSD matrices for both notches were computed. Later, the equivalent stress–PSD was computed according to Equation (6), and subsequently the damage D and the fatigue life T_{sim} were calculated using Equations (8) and (13). The numerical fatigue results are presented in the next Section 5 and compared with the experimental test results.

5. Experimental Validation

The testing set-up used is proposed in Figure 13. The aim of the experimental test was the validation of the numerical FRF and the numerical fatigue life under random variable amplitude. The evaluation was accomplished, conducting two distinct and uncorrelated testing campaigns, one around each resonant mode. For the second mode, 11 specimens were used (*C*12, *C*13, *C*14, *C*15, *C*16, *C*17, *C*18, *C*19, *C*21, *C*27, and *C*28), while for the fourth mode, 9 specimens were used (*C*01, *C*02, *C*03, *C*04, *C*05, *C*06, *C*07, *C*08, and *C*10).

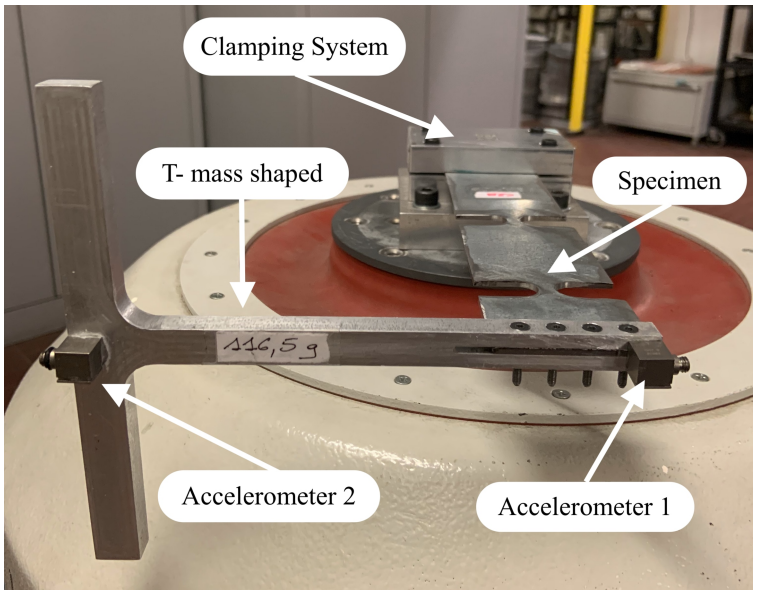

Figure 13. Experimental testing set-up.

The frequency sweep range for the second mode is between 30 Hz and 50 Hz, while for the fourth mode, it is between 100 Hz and 130 Hz. The acceleration is 0.1 g for both sweep tests. Figure 14 reports all the experimental signals for each accelerometer. The peaks of acceleration amplitude on the frequency resonances encounter a large distribution of peaks for all the specimens tested, from 0.7 g with $C12$ to 1.8 g with $C13$ for the second mode, and from 1.42 g with $C03$ to 2.56 g with $C05$ for the fourth mode. In addition, it is important to note that specimens $C02$ and $C04$ present non-linear behaviour. This might be produced by a small plasticity zone located in the notches of the specimens. Due to this non-linearity, specimen $C02$ and $C04$ were discarded for the fatigue analysis.

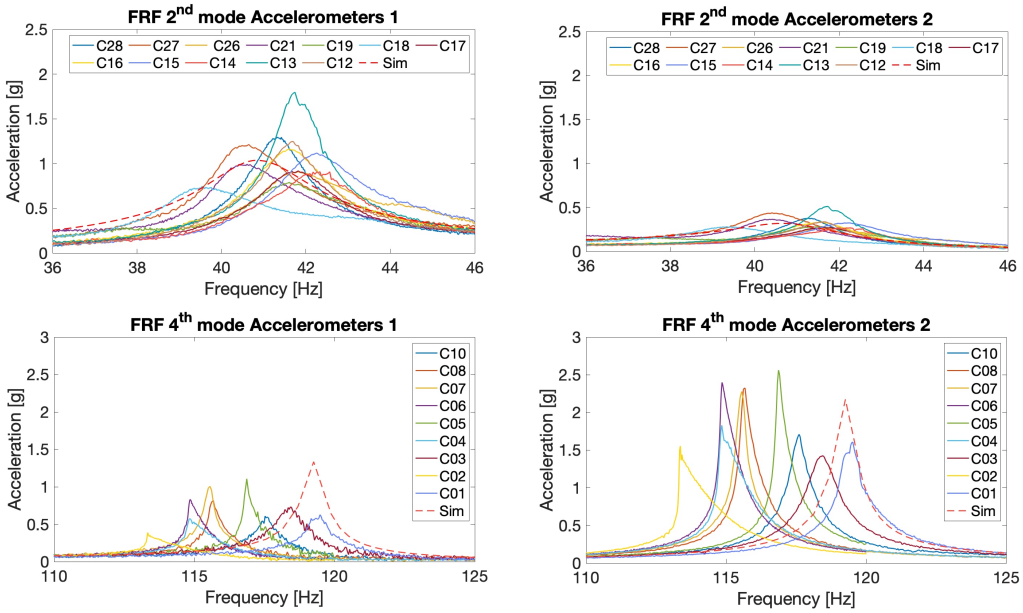

Figure 14. Experimental output acceleration from both accelerometers for mode 2 and mode 4.

The comparison with the numerical FRF was accomplished using the average of the maximum acceleration values across all test pieces, for each mode. Table 10 reports the average of the maximum acceleration from the two accelerometers for modes 2 and 4. The maximum relative error between average peaks and numerical peaks, expressed as $(f_{exp} - f_{sim})/f_{exp} \times 100$, is lower than 5%.

Table 10. Average experimental acceleration amplitude for the second and fourth modes.

Mode	Accelerometer 1 [g]	Accelerometer 2 [g]
1	1.1	0.3
2	0.7	2

In addition, strain gauges were used to measure the experimental strain for the second and fourth modes on the specimen, which were compared with the numerical ones, as shown in Figure 15. The experimental deformation results matched the numerical ones with good agreement.

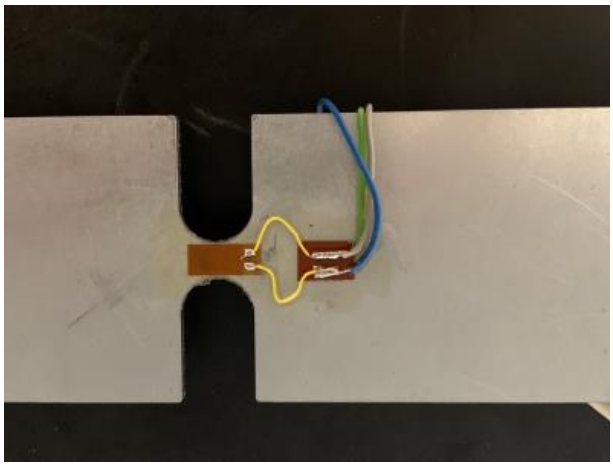

Figure 15. Strain gauge installation.

Random Loading Tests

After determining the experimental resonant frequencies, each sample was subjected to a bandwidth-limited white noise PSD within a 20 Hz frequency range, centered on the resonant frequency of its corresponding mode. The PSD input load levels were selected based on those applied in the numerical simulations, as detailed in Table 9. The test was stopped either by the failing of the specimen or after 8 h, the duration for which the specimen was considered to have survived.

In Figure 16, the comparison between the numerical time to failure T_{sim} obtained with the numerical method of narrow band model and the experimental time to failure T_{exp} is reported. The solid line indicates $T_{sim} = T_{exp}$, the dashed lines correspond to T_{sim}/T_{exp} equal to 0.5 and 2, and the dash–dot lines correspond to T_{sim}/T_{exp} equal to 0.3 and 3. For the experimental case, the solid line is linked to the average time-to-failure results for each load level.

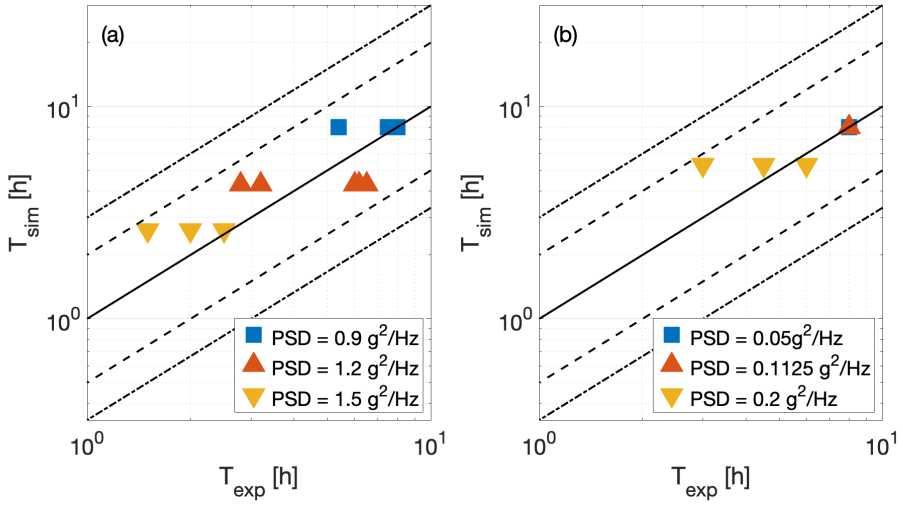

Figure 16. Testing results for the second mode (**a**) and the fourth mode (**b**).

In light of the results, for mode 2, under 0.9 g^2/Hz, the time to failure passes 8 h. At 1.5 g^2/Hz, the average life before failure is approximately 2 h. At 1.2 g^2/Hz, the results have a large distribution from 3 h to 6.5 h. This large distribution could be caused by a non-perfect clamping of the specimen at the top of the shaker. In the case of mode 4, any specimen tested encountered a fatigue failure below 0.115 g^2/Hz, while, at 0.2 g^2/Hz, the average life of the system is 4.41 h. All the results are within the dashed line. For the second mode, the numerical model tends to overestimate the time to failure, especially for

the load levels 0.9 g^2/Hz and 1.5 g^2/Hz, while in the fourth mode, the numerical model shows a better correlation, considering the good prediction of the time to failure for the load levels 0.05 g^2/Hz and 0.1125 g^2/Hz.

Figure 17a,b show the different failure modes that occur for each mode shape. When the specimen is loaded around the second resonant frequency, the failure surface has an irregular shape. The crack propagates in a diagonal direction with respect to the transversal specimen plane, due to the combination of shear and normal stresses. On the contrary, when the specimen is loaded around mode 4, the surface is perfectly perpendicular to the transversal specimen plane, which proves that the specimen is experiencing normal stress because of a fully bending deformation.

(**a**) (**b**)

Figure 17. Failure surface for (**a**) mode 2 and (**b**) mode 4.

6. Conclusions

A simple and reliable test bench for random multi-axial fatigue testing of specimens is presented.

In multi-axial random fatigue testing, the limitations in terms of experimental equipment have led many researchers to propose solutions, which differ in terms of the testing equipment, specimen geometry, and type of excitation.

This paper presents a new set-up and procedure for testing multi-axial random fatigue, which enables obtaining bending–torsion stress states by means of vibration tests with a cantilever beam, with uni-axial excitation. A finite element model is used to investigate the dynamic behaviour of the system and the stress distribution on the notched section of a specifically shaped specimen. The modal analysis allows the identification of the resonances and mode shapes. This information is used to select the frequency range to be applied in random uni-axial excitation to obtain the desired ratio between normal and shear stress in the specimen. The analysis conducted by the authors reveals how the T-mass could affect and change the dynamic behaviour of the specimen. In particular, it is worth pointing out the presence of a torsional deformation in all the mode shapes, considered to be remarkable torsional deformation on the second natural mode, and a bending deformation, with little torsion deviation, on the fourth mode. This information also provides the data required for the numerical estimation of the random fatigue life in multi-axial conditions. An experimental validation, by means of an harmonic acceleration test, was run. The comparison of the numerical and experimental results, in two different conditions of shear/normal stress ratio, show a good agreement. Furthermore, the experimental results of fatigue tests under random vibration loading, show that the equivalent stress in the

second mode is lower than that in the fourth mode. Consequently, to have the same fatigue cycles, the PSD load levels for mode 4 should be lower than for mode 2. Further investigations are planned for evaluating micro-structural differences between the fracture surface of the two modes, and identification of the critical plane direction. The definition of a new damage model for this case study is also ongoing, which will be compared with the NarrowBand damage approach.

Author Contributions: Conceptualization, methodology, software, validation, formal analysis, investigation, resources, data curation, writing—original draft preparation, L.C.; writing—review and editing, V.D., R.S. (Raffaella Sesana), C.D. and R.S. (Roger Serra); supervision, project administration, funding acquisition, R.S. (Roger Serra), C.D. and R.S. (Raffaella Sesana). All authors have read and agreed to the published version of the manuscript.

Funding: This research was 50% funded for by the Centre Val de Loire region, Convention n°2021 00148892.

Data Availability Statement: All the data can be made available upon request.

Conflicts of Interest: The authors declare no conflicts of interest.

References

1. Schijve, J. *Fatigue of Structures and Materials*; Springer: Berlin/Heidelberg, Germany, 2009.
2. Sonsino, C.M. Multiaxial fatigue life response depending on proportionality grade between normal and shear strains/stresses and material ductility. *Int. J. Fatigue* **2020**, *135*, 105468. [CrossRef]
3. *ASTM E466-21*; Standard Practice for Conducting Force Controlled Constant Amplitude Axial Fatigue Tests of Metallic Materials. ASTM International: West Conshohocken, PA, USA, 2021.
4. *ISO 1099:2017*; Metallic Materials—Fatigue Testing—Axial Force-Controlled Method. International Organization for Standardization: Berlin, Germany, 2017.
5. *DIN 50100:2016-12*; Load Controlled Fatigue Testing—Execution and Evaluation of Cyclic Tests at Constant Load Amplitudes on Metallic Specimens and Components. Deutsches Institut für Normung: Geneva, Switzerland, 2016.
6. Fatemi, A.; Yang, L. Cumulative fatigue damage and life prediction theories: A survey of the state of the art for homogeneous materials. *Int. J. Fatigue* **1998**, *20*, 9–34. [CrossRef]
7. Liu, Z.; Wang, M.; Guo, P.; Gao, D.; Gao, Y. Numerical and Experimental-Based Framework for Fuel Cell System Fatigue Analysis in Frequency Domain. *Machines* **2025**, *13*, 18. [CrossRef]
8. Shen, K.; Ma, F.; Yuan, J.; Zhang, M. A Damage Combination Method for Fatigue Analysis of Pressure Equipment in Floating Nuclear Power Plants. *J. Mar. Sci. Eng.* **2025**, *13*, 236. [CrossRef]
9. Mršnik, M.; Slavič, J.; Boltežar, M. Multiaxial vibration fatigue—A theoretical and experimental comparison. *Mech. Syst. Signal Process.* **2016**, *76–77*, 409–423. [CrossRef]
10. Carpinteri, A.; Spagnoli, A.; Vantadori, S. A review of multiaxial fatigue criteria for random variable amplitude loads. *Fatigue Fract. Eng. Mater. Struct.* **2017**, *40*, 1007–1036. [CrossRef]
11. Braccesi, C.; Morettini, G.; Cianetti, F.; Palmieri, M. Development of a new simple energy method for life prediction in multiaxial fatigue. *Int. J. Fatigue* **2018**, *112*, 1–8. [CrossRef]
12. Pitoiset, X.; Preumont, A. Spectral methods for multiaxial random fatigue analysis of metallic structures. *Int. J. Fatigue* **2000**, *22*, 541–550. [CrossRef]
13. Habtour, E.; Connon, W.; Pohland, M.; Stanton, S.; Paulus, M.; Dasgupta, A. Review of Response and Damage of Linear and Nonlinear Systems Under Multiaxial Vibration. *Shock Vib.* **2014**, *2014*, 294271. [CrossRef]
14. Appert, A.; Gautrelet, C.; Khalij, L.; Troian, R. Development of a test bench for vibratory fatigue experiments of a cantilever beam with an electrodynamic shaker. In Proceedings of the 12th International Fatigue Congress, Poitiers, France, 27 May–1 June 2018.
15. Ghielmetti, C.; Ghelichi, R.; Guagliano, M.; Ripamonti, F.; Vezzù, S. Development of a fatigue test machine for high frequency applications. *Procedia Eng.* **2011**, *10*, 2892–2897. [CrossRef]
16. Paulus, M.; Dasgupta, A.; Habtour, E. Life estimation model of a cantilevered beam subjected to complex random vibration. *Fatigue Fract. Eng. Mater. Struct.* **2012**, *35*, 1058–1070. [CrossRef]
17. de M. Teixeira, G. Random vibration fatigue analysis of a notched aluminum beam. *Int. J. Mech. Eng. Autom.* **2015**, *2*, 425–441.
18. Whiteman, W.; Berman, M. Fatigue Failure Results for Multi-Axial Versus Uniaxial Stress Screen Vibration Testing. *Shock Vib.* **2002**, *9*, 319–328. [CrossRef]
19. Whiteman, W.; Berman, M. Inadequacies in Uniaxial Stress Screen Vibration Testing. *J. IEST* **2005**, *44*, 20–23. [CrossRef]

20. French, M.; Handy, R.; Cooper, H. A Comparison of simultaneous and sequential single axis durability testing. *Exp. Tech.* **2006**, *30*, 32–37. [CrossRef]
21. Nath, N.; Aglietti, G.S. Study the effect of tri-axis vibration testing over single-axis vibration testing on a satellite. In Proceedings of the 2022 IEEE Aerospace Conference (AERO), Big Sky, MT, USA, 5–12 March 2022; pp. 1–10. [CrossRef]
22. Zheng, R.; Liu, C.; Feng, G.; Wei, X.; Chen, H. Spectral decoupled correction algorithm for multi-input multi-output random vibration control. *J. Vib. Control* **2024**, *30*, 3797–3805. [CrossRef]
23. Marques, E.J.; Benasciutti, D.; Niesłony, A.; Slavič, J. An Overview of Fatigue Testing Systems for Metals under Uniaxial and Multiaxial Random Loadings. *Metals* **2021**, *11*, 447. [CrossRef]
24. Morettini, G.; Braccesi, C.; Cianetti, F.; Razavi, N. Design and implementation of new experimental multiaxial random fatigue tests on astm-a105 circular specimens. *Int. J. Fatigue* **2021**, *142*, 105983. [CrossRef]
25. Morettini, G.; Braccesi, C.; Cianetti, F. Experimental multiaxial fatigue tests realized with newly developed geometry specimens. *Fatigue Fract. Eng. Mater. Struct.* **2019**, *42*, 827–837. [CrossRef]
26. Claudio, R.; Reis, L.; Freitas, M. Biaxial high cycl fatigue life assessment of ductile aluminium cruciform specimens. *Theor. Appl. Fract. Mech.* **2014**, *73*, 82–90. [CrossRef]
27. George, T.; Seidt, J.; Shen, M.H.; Nicholas, T.; Cross, C.J. Development of a novel vibration-based fatigue testing methodology. *Int. J. Fatigue* **2004**, *26*, 477–486. [CrossRef]
28. Daborn, P.M.; Ind, P.; Ewins, D. Enhanced ground-based vibration testing for aerodynamic environments. *Mech. Syst. Signal Process.* **2014**, *49*, 165–180. [CrossRef]
29. Łagoda, T.; Macha, E.; Nieslony, A. Fatigue life calculation by means of the cycle counting and spectral methods under multiaxial random loading. *Fatigue Fract. Eng. Mater. Struct.* **2005**, *28*, 409–420.
30. Nguyen, N.; Bacher-Höchst, M.; Sonsino, C.M. A frequency domain approach for estimating multiaxial random fatigue life. *Mater. Werkst.* **2011**, *42*, 904–908. [CrossRef]
31. Zanellati, D.; Benasciutti, D.; Tovo, R. An innovative system for uncoupled bending/torsion tests by tri-axis shaker: Numerical simulations and experimental results. *MATEC Web Conf.* **2018**, *165*, 16006. [CrossRef]
32. Česnik, M.; Slavič, J.; Boltežar, M. Uninterrupted and accelerated vibrational fatigue testing with simultaneous monitoring of the natural frequency and damping. *J. Sound Vib.* **2012**, *331*, 5370–5382. [CrossRef]
33. Rognon, H. Comportement en Fatique sous Environnement Vibratoire: Prise en Compe de la Plasticite au sein des Methodes Spectrales. Ph.D. Thesis, Ecole Centrale Paris, Châtenay-Malabry, France, 2013.
34. Bendat, J.; Piersol, A. *Random Data: Analysis and Measurement Procedures*; Wiley: Hoboken, NJ, USA, 2011. [CrossRef]
35. Maia, N.; Silva, J. *Theoretical and Experimental Modal Analysis*; Research Studies Press: Newton, MA, USA, 1997.
36. Niesłony, A.; Macha, E. *Spectral Method in Multiaxial Random Fatigue*; Zeszyty Naukowe. Mechanika/Politechnika Opolska; Springer: Berlin/Heidelberg, Germany, 2005; pp. 113–134.
37. Socie, D.; Marquis, G. *Multiaxial Fatigue*; SAE International: Warrendale, PA, USA, 1999.
38. Česnik, M.; Slavič, J.; Čermelj, P.; Boltežar, M. Frequency-based structural modification for the case of base excitation. *J. Sound Vib.* **2013**, *332*, 5029–5039. [CrossRef]
39. Kranjc, T.; Slavič, J.; Boltežar, M. A comparison of strain and classic experimental modal analysis. *J. Vib. Control* **2014**, *22*, 371–381. [CrossRef]
40. Mršnik, M.; Slavič, J.; Boltežar, M. Vibration fatigue using modal decomposition. *Mech. Syst. Signal Process.* **2018**, *98*, 548–556. [CrossRef]
41. Jang, J.; Park, J.W. Simplified vibration PSD synthesis method for MIL-STD-810. *Appl. Sci.* **2020**, *10*, 458. [CrossRef]
42. Pitoiset, X.; Rychlik, I.; Preumont, A. Spectral methods to estimate local multiaxial fatigue failure for structures undergoing random vibrations. *Fatigue Fract. Eng. Mater. Struct.* **2001**, *24*, 715–727. [CrossRef]
43. Miner, M.A. Cumulative Damage in Fatigue. *J. Appl. Mech.* **2021**, *12*, A159–A164. [CrossRef]
44. Mršnik, M.; Slavič, J.; Boltežar, M. Frequency-domain methods for a vibration-fatigue-life estimation—Application to real data. *Int. J. Fatigue* **2012**, *47*, 8–17. [CrossRef]
45. Milella, P.P. *Fatigue and Corrosion in Metals*; Springer Science & Business Media: Berlin/Heidelberg, Germany, 2012.
46. Nagulapalli, V.; Gupta, A.; Fan, S. Estimation of fatigue life of aluminum beams subjected to random vibration. In *Conference Proceedings of the Society for Experimental Mechanics Series*; Springer: Berlin/Heidelberg, Germany, 2007.